Invited Paper

AlGaN-based high-performance metal–semiconductor–metal photodetectors

Mutlu Gökkavas [a,*], Serkan Butun [a], Turgut Tut [a], Necmi Biyikli [b], Ekmel Ozbay [a]

[a] *Nanotechnology Research Center, Department of Physics, Department of Electrical and Electronics Engineering, Bilkent University, Bilkent, Ankara 06800, Turkey*
[b] *Department of Electrical and Computer Engineering, Virginia Commonwealth University, 601 West Main Street, Richmond, VA 23284, USA*

Abstract

Design, structure growth, fabrication, and characterization of high performance AlGaN-based metal–semiconductor–metal (MSM) photodetectors (PD) are reported. By incorporating AlN nucleation and buffer layers, the leakage current density of GaN MSM PD was reduced to 1.96×10^{-10} A/cm^2 at a 50 V bias, which is four orders of magnitude lower compared to control devices. A 229 nm cut-off wavelength, a peak responsivity of 0.53 A/W at 222 nm, and seven orders of magnitude visible rejection was obtained from Al$_{0.75}$Ga$_{0.25}$N MSM PD. Two-color monolithic AlGaN MSM PD with excellent dark current characteristics were demonstrated, where both detectors reject the other detector spectral band with more than three orders of magnitude. High-speed measurements of Al$_{0.38}$Ga$_{0.62}$N MSM PD resulted in fast responses with greater than gigahertz bandwidths, where the fastest devices had a 3-dB bandwidth of 5.4 GHz.
© 2007 Elsevier B.V. All rights reserved.

Keywords: Photodetector; Ultraviolet; Photonics; AlGaN; GaN; MOCVD; Nitride

1. Introduction

The detection of ultraviolet (UV) radiation is important for a wide range of traditional and emerging military and civil applications which include flame detection for fire alarms, engine combustion monitoring, furnace monitoring and missile warning; secure non-line-of-sight and space communications, environmental monitoring, UV emitter calibration and detection of chemical and biological warfare agents [1–3]. Ultraviolet detection has traditionally been accomplished by photomultiplier tubes (PMT) and Si photodiodes. Photomultiplier tubes exhibit high gain

and low noise; however, they are bulky, expensive instruments with high power requirements. With the availability of high quality AlGaN ternary material growth [4–10], Al$_x$Ga$_{1-x}$N based materials emerged as suitable semiconductor candidates for detecting ultraviolet (UV) spectrum, since the band gap of Al$_x$Ga$_{1-x}$N materials covers the entire mid-UV and near-UV spectrum by varying the Al concentration. Within the last decade, many groups contributed to the performance of AlGaN photodetectors. The first photovoltaic (photodiode) III-nitride based photodetector was demonstrated by Khan et al. [11] in 1993. Shortly after, the first AlGaN based solar-blind photodetectors were demonstrated in 1996 [12,13]. These detectors are unique in the sense that they are not responsive to the background radiation from the sun, since the solar radiation within their spectral band ($\lambda < 280$ nm) is

---

* Corresponding author.
  E-mail address: mgokkavas@fen.bilkent.edu.tr (M. Gökkavas).

filtered by the ozone layer before reaching the lower levels of the atmosphere. Therefore solar-blind detectors are immune to solar noise, and can only detect man-made signals. It soon became evident that solar-blind AlGaN photodetectors can become alternatives for the PMT and Si technologies with their intrinsic spectral selectivity. Following the first reports on photoconductive devices, Schottky [14–16], p-i-n [17–23], MSM [24,25], and avalanche photodiodes [26,27] have successfully been demonstrated.

The metal–semiconductor–metal (MSM) photodetector is a type of Schottky barrier detector, which cannot operate at zero bias. However, it presents the potential for very high speed of operation. In addition, MSM type photodetectors simplify the growth and fabrication processes as the necessity for contacts and doped ohmic layers is eliminated [28]. In this paper, we present our research efforts on the design, fabrication and characterization of high performance AlGaN-based MSM photodetectors. GaN MSM photodetectors with record low dark current density and solar-blind AlGaN MSM photodetectors with record UV/visible contrast ratio, low cut-off wavelength and 3-dB bandwidth are demonstrated. We also demonstrated monolithic two-color MSM photodetectors.

2. Sample design, growth and fabrication

The metal–semiconductor–metal photodetector structures described in this study were all grown on c-face (0 0 0 1) sapphire substrates by low-pressure metalorganic chemical vapor deposition (MOCVD). Hydrogen was used as the carrier gas, and trimethyl-gallium (TMGa), trimethylaluminum (TMAl), and ammonia (NH$_3$) were used as the Ga, Al, and N sources, respectively. Prior to the epitaxial growth of all structures, sapphire substrates were annealed at 1100 °C for 10 min to remove surface contamination.

Table 1 shows the layer structures of GaN MSM photodetectors. Two samples were grown for a comparison of using AlN nucleation and buffer layers versus GaN nucleation layer. Sample 1a includes a 15 nm low temperature (840 °C) AlN nucleation layer followed by a 0.5 μm high temperature (1150 °C) AlN buffer layer and a 0.5 μm unintentionally doped GaN layer. Sample 1b consists of a 15 nm low temperature (500 °C) GaN nucleation layer followed by a 0.5 μm GaN layer. In order to have a fair comparison, top GaN layer growth parameters were identical for both samples: reactor pressure 200 mbar, growth temperature 1070 °C, H$_2$ carrier gas, and growth rate about 2 μm/h.

Table 1
GaN MSM photodetector structures

Sample 1a		Sample 1b	
GaN layer grown on AlN buffer and nucleation layers		GaN layer grown on GaN nucleation layer	
Material	Thickness	Material	Thickness
GaN	0.5 μm		
AlN buffer layer	0.5 μm	GaN	0.5 μm
AlN nucleation layer	∼15 nm	GaN nucleation layer	∼15 nm
Sapphire substrate	∼300 μm	Sapphire substrate	∼300 μm

Samples 2a and 2b were designed for the fabrication of low cut-off wavelength solar-blind MSM photodetectors. The corresponding layer structures are shown in Table 2. For sample 2a, a thin (∼50 nm) low temperature AlN nucleation layer and a ∼0.7 μm high temperature AlN buffer layer were grown prior to the growth of the unintentionally doped ∼0.6 μm Al$_{0.75}$Ga$_{0.25}$N absorption layer. For sample 2b, a thin (<100 nm) low temperature AlN nucleation layer was followed by the growth of a 2 μm unintentionally doped Al$_{0.6}$Ga$_{0.4}$N layer.

The structure shown in Table 3 was grown for the fabrication of two-color monolithic AlGaN MSM photodetectors. The operation principle of the two-color detectors is explained in Section 4. The structure basically consists of an absorbing spectral-filter-layer sandwiched between two active detector layers: firstly, a 15 nm-thick AlN nucleation layer was deposited at 550 °C. Thereafter, the reactor temperature was ramped to 1130 °C, pressure was ramped down to 25 mbar and a 0.4 μm-thick bottom detector layer ($x_b = 0.5$) was grown, followed by another nucleation layer of 15 nm-thick AlN at 550 °C in order to prevent dislocations and cracks in the subsequent 1 μm-thick filter layer ($x_f = 0.25$). The growth conditions for the filter layer were as follows: reactor pressure 50 mbar, growth temperature 1080 °C, H$_2$ carrier gas, and growth

Table 2
Low cut-off wavelength AlGaN MSM photodetector structures

Sample 2a		Sample 2b	
Material	Thickness	Material	Thickness
Al$_{0.75}$Ga$_{0.25}$N	0.6 μm		
AlN buffer layer	0.7 μm	Al$_{0.6}$Ga$_{0.4}$N	2 μm
AlN nucleation layer	∼50 nm	AlN nucleation layer	<100 nm
Sapphire substrate	∼300 μm	Sapphire substrate	∼300 μm

Table 3

Two-color AlGaN MSM photodetector structure

Sample 3	
Material	Thickness
$Al_{0.2}Ga_{0.8}N$ top detector layer	0.25 μm
$Al_{0.27}Ga_{0.73}N$ spectral filter layer	1 μm
AlN nucleation layer	∼15 nm
$Al_{0.5}Ga_{0.5}N$ bottom detector layer	0.4 μm
AlN nucleation layer	∼15 nm
Sapphire substrate	∼300 μm

Table 4

High-speed solar-blind AlGaN MSM photodetector structure

Sample 4	
Material	Thickness
$Al_{0.38}Ga_{0.62}N$ detector layer	1 μm
GaN buffer layer	2 μm
AlN nucleation layer	<100 nm
Sapphire substrate	∼300 μm

rate approximately 2 μm/h. Finally, the 0.25 μm-thick top detector layer ($x_t = 0.2$) was grown at 1080 °C.

For high-speed solar-blind operation, an $Al_{0.38}Ga_{0.62}N$ MSM photodetector structure was designed as shown in Table 4. Following a thin AlN nucleation layer, a 2 μm-thick GaN buffer layer was grown to reduce the defect density of the subsequent 1 μm-thick $Al_{0.38}Ga_{0.62}N$ active detector layer. The 38% Al-concentration was chosen in order to achieve solar-blindness.

Metal–semiconductor–metal photodetectors were fabricated with a four-step microwave compatible process in a class-100 clean room environment. First, 100 Å Ni/1000 Å Au interdigitated fingers were deposited on the active detector layers. Finger spacing and width varied between 1.5 μm and 10 μm. Subsequently, 100 μm × 100 μm and 400 μm × 400 μm device mesas along with active areas were defined by CCl_2F_2 based reactive ion etching (RIE). The MSM detectors were passivated with a 120 nm thick Si_3N_4 layer, grown by a plasma enhanced chemical vapor deposition (PECVD) system. The Si_3N_4 layer was also used as an antireflection layer as well as for protecting the metal fingers. Finally, 100 Å Ti/4000 Å Au interconnect pads were deposited. Fig. 1 shows several microphotographs of completed MSM photodetectors.

3. GaN MSM photodetectors

There have only been a few reports regarding relatively low dark current devices fabricated on GaN.

To our knowledge, the best result was around 10 pA at 100 V bias [29]. In this section, we present our results on GaN MSM photodetectors with very low dark current densities. The two samples shown in Table 1 were grown as described in Section 2. X-ray diffraction (XRD) measurements were performed in the Semiconductor Technologies Advanced Research Laboratory of Gazi University, Ankara in order to compare the crystal qualities of samples 1a and 1b. Fig. 2 illustrates the normalized XRD intensities of both samples at GaN 0 0 2 peak position. Sample 1a has a full-width-at-half-maximum (FWHM) of 148 arcsec, whereas sample 1b has a FWHM of 360 arcsec. These measurements indicate the better crystal quality of sample 1a.

Fabrication of photodetectors was completed as described in Section 2. In addition, we measured the sheet resistivities of samples 1a and 1b using standard transmission line measurements. The sheet resistances of samples 1a and 1b were found as 3.16×10^{11} Ω/sq. and 5.8×10^7 Ω/sq., respectively. Current–voltage (*I–V*) characterization of the fabricated MSM photodetectors was carried out using a Keithley 6517A high-resistance electrometer with low noise triax cables in a grounded shielded cage. The devices fabricated on sample 1a exhibited extremely low dark currents, while those fabricated on sample 1b exhibited relatively higher dark currents, typical for devices fabricated on GaN. No breakdown was observed for bias voltages as high as 200 V for 200 μm × 200 μm active area detectors fabricated on both samples. Fig. 3 compares the dark *I–V* curves of 10 μm finger width/spacing devices from the two samples. The dark current measured from devices fabricated on sample 1a remains below 1 pA up to a 100 V bias voltage. The dark current density (at 50 V bias) of a device fabricated on sample 1a is calculated as 1.96×10^{-10} A/cm^2. In comparison, the 50 V dark current density calculated for a similar device fabricated on sample 1b is 8.1×10^{-6} A/cm^2, which corresponds to four orders of magnitude improvement.

Spectral photocurrent characteristics of the fabricated devices were measured by way of using a Xe lamp and monochromator assembly. The narrow spectral output of the monochromator was modulated by an optical chopper, coupled into a multimode UV-enhanced fiber, and delivered to the device-under-test on a probe station. The resulting photocurrent was recorded as a function of wavelength by using a lock-in amplifier. The spectral power density of the light at the output of the fiber was measured by a NIST-traceable calibrated Si photodetector. For photocurrent measurements, 200 μm × 200 μm area devices with 3 μm/3 μm finger width/
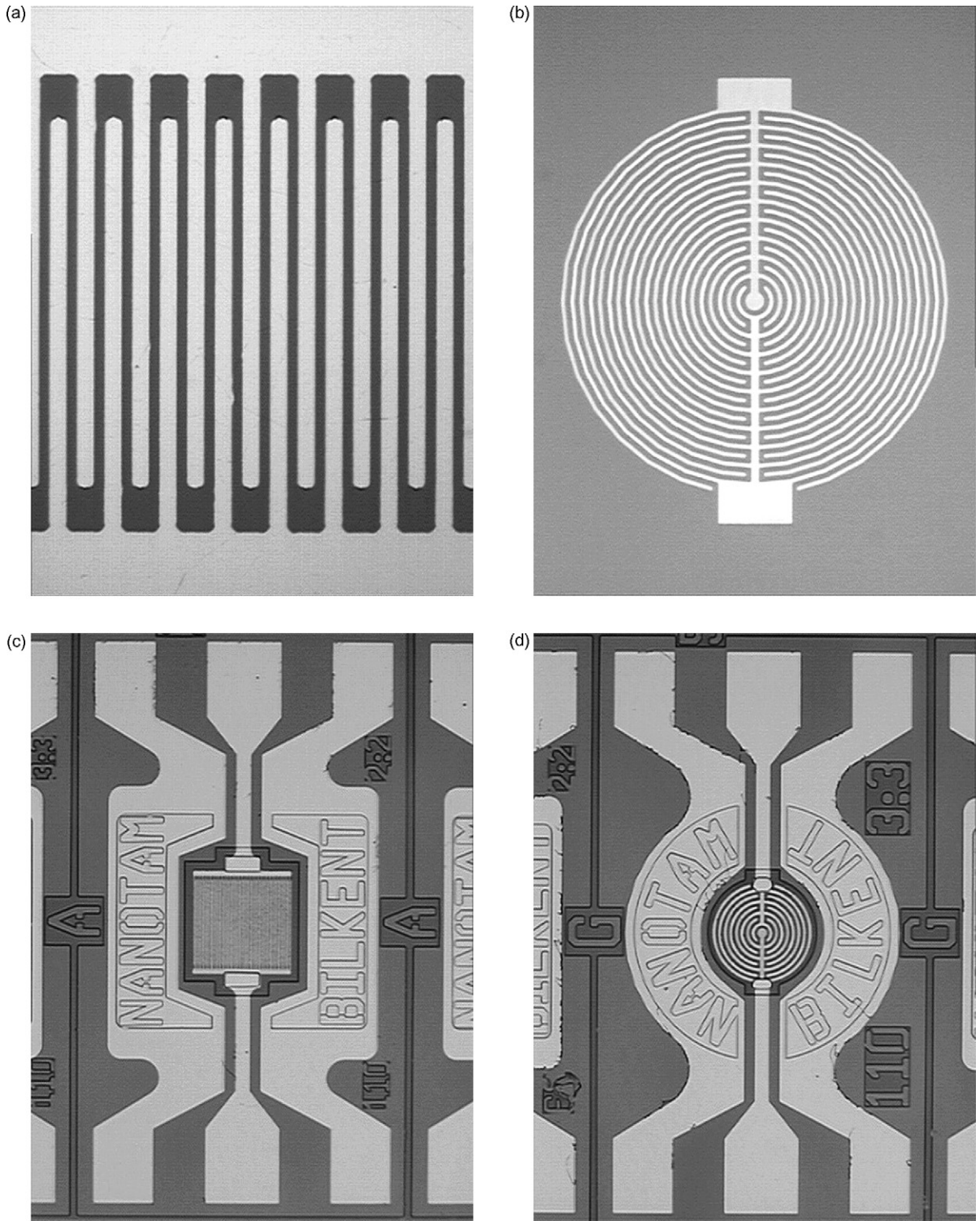
Fig. 1. Microphotographs of MSM photodetectors: (a) detail of interdigitated fingers; (b) circular interdigitated fingers; (c and d) completed MSM photodetectors.
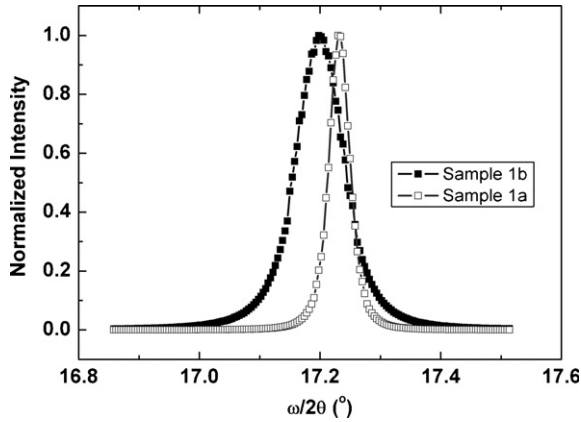
Fig. 2. X-ray diffraction intensities of samples 1a and 1b at GaN 0 0 2 peak position.
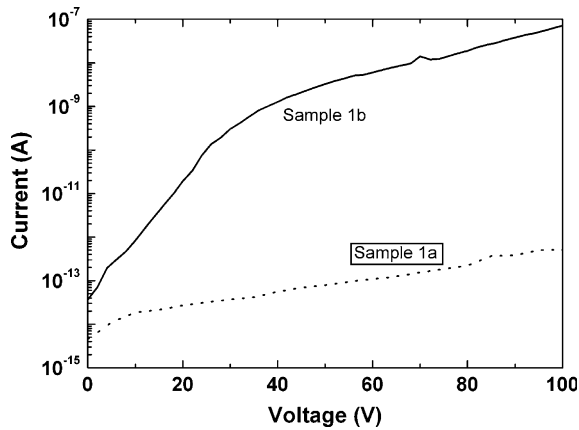

Fig. 3. Current–voltage characteristics of 200 μm × 200 μm GaN MSM photodetectors with 10 μm/10 μm finger width/spacing fabricated on sample 1a (grown on top of AlN nucleation and buffer layers) and sample 1b (grown on top of GaN nucleation layer).

spacing were used. Fig. 4 shows the spectral dependence of the photoresponse for both devices. Devices from both samples exhibited a sharp cut-off at 365 nm, while the peak of the photoresponse was observed at 360 nm. Device peak responsivity increased with applied voltage and reached 101.80 A/W for sample 1a and 88.63 A/W for sample 1b at 50 V bias. These very high responsivity values indicate that devices have a gain of about 700 that can be attributed to the photoconductive gain mechanism in MSM detectors. The photoconductive gain in AlGaN MSM PDs can be explained by the presence of hole-trapping sites due to threading dislocations [30]. Holes are accumulated at the trap sites, increasing the electron injection at the cathode. This injection results in photoconductive gain which is proportional to the electric field between the electrodes.

Fig. 5 displays the 355 nm/400 nm photoresponse contrast for both devices as a function of bias voltage. It
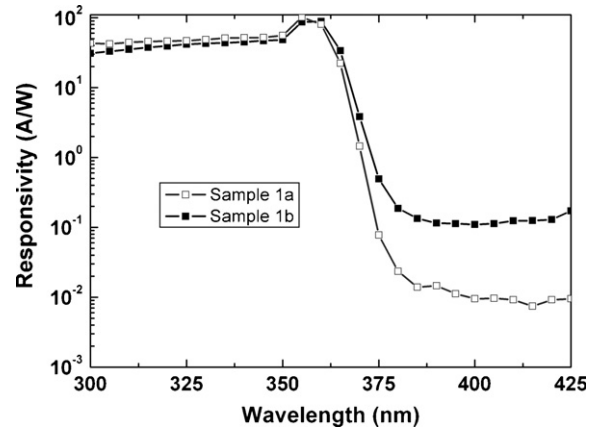

Fig. 4. Spectral responsivity curves of 200 μm × 200 μm GaN MSM photodetectors with 3 μm/3 μm finger width/spacing fabricated on sample 1a (grown on top of AlN nucleation and buffer layers) and sample 1b (grown on top of GaN nucleation layer) measured at 50 V.
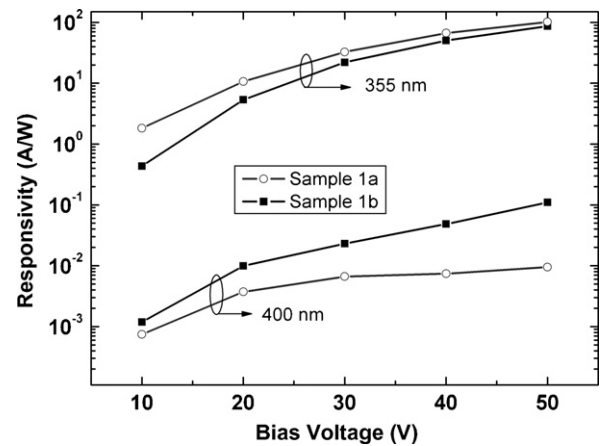

Fig. 5. 355 nm- and 400 nm-responsivity curves of 200 μm × 200 μm GaN MSM photodetectors fabricated on samples 1a and 1b as a function of bias voltage.
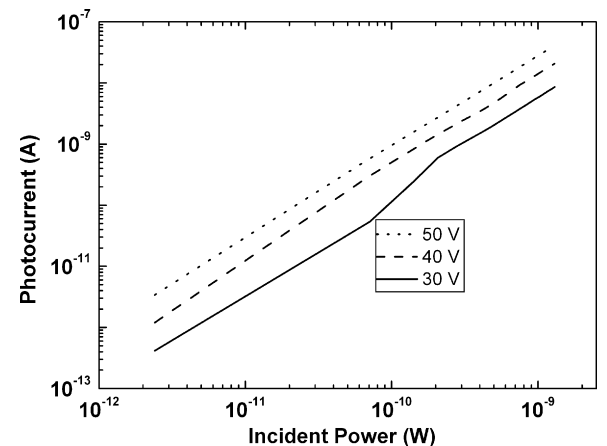

Fig. 6. Measured photocurrent of a 200 μm × 200 μm device on sample 1a as a function of optical power and bias voltage.

is seen that UV/visible rejection is about four orders of magnitude for sample 1a and three orders of magnitude for sample 1b.

Finally, a low optical power responsivity measurement was performed in order to determine the minimum detectable optical power. A series of neutral density filters were used to vary the incident optical power in the few pW to 1 nW range. As expected, it was possible to detect very low level powers because of the large gain and low dark current values for devices fabricated on sample 1a. As shown in Fig. 6, measured dc photocurrent of a device on sample 1a is well above dark current (in Fig. 3) for incident optical powers as low as 3 pW.

4. Low cut-off wavelength AlGaN MSM photodetectors

Since it is difficult to grow high quality and crack-free high Al content material, there are only a few low cut-off wavelength photodetectors reported in the literature. The best results were reported by Razeghi et al. where the cut-off wavelength was 235 nm [31]. In this section, we present our results on the fabrication and characterization of deep UV MSM photodetectors based on $Al_xGa_{1-x}N$ epilayers, where $x \geq 0.6$. The two samples shown in Table 2 were grown and MSM photodetectors were fabricated as described in Section 2.

Fig. 7 shows the spectral transmission measurements of samples 2a and 2b prior to the fabrication, which was used to determine the Al concentration. Sample 2a exhibited a 225 nm sharp cut-off, indicating an Al concentration of approximately 75%, while sample 2b exhibited a 243 nm cut-off indicating a 60% Al
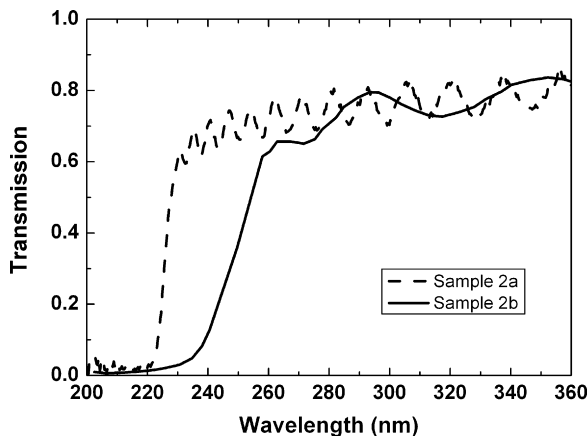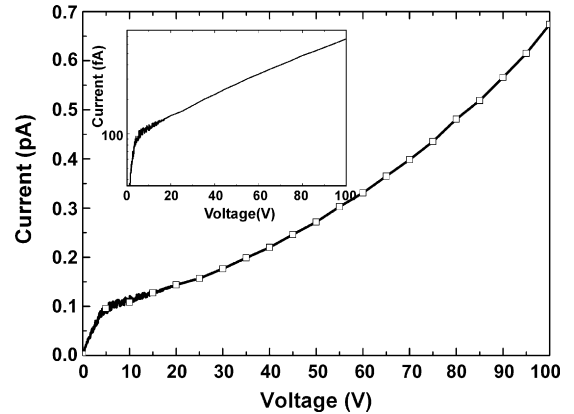

Fig. 8. Dark current measurement of a 200 μm × 200 μm MSM photodetector fabricated on sample 2a ($Al_{0.75}Ga_{0.25}N$). Inset: same graph at semilog scale.

concentration. Both spectra have Fabry–Perot oscillations, implying the high quality of the AlGaN layers.

Current–voltage measurements were performed as described in Section 3. The resulting devices exhibited extremely low dark currents and very high breakdown voltages. Fig. 8 shows the *I–V* curve of a 4 μm finger width/spacing 200 μm × 200 μm device on sample 2a. The dark current is below 700 fA up to ±100 V bias voltage, and the dark current density at 50 V bias is 4×10^{-9} A/cm^2. Even under high bias voltages like 350 V, dark current does not exceed 100 pA. These low dark currents and high breakdown voltages show the high quality of our $Al_{0.75}Ga_{0.25}N$ layers. For sample 2b, the dark current performance was even better, where dark current was less than 100 fA up to ±100 V bias voltage, the 50 V-dark current density was 5.8×10^{-10} A/cm^2, and no sign of breakdown was observed up to 300 V [32].

Spectral responsivity measurements were performed as described in Section 3. The resulting responsivity curve as a function of applied bias voltage for a 400 μm × 400 μm device with 2 μm/3 μm finger width/spacing fabricated on sample 2a is shown in Fig. 9 for 20 V bias. Devices exhibited a sharp cut-off at 229 nm and a peak photoresponse at 222 nm, which was in good agreement with the transmission measurements. Device responsivity increased with applied voltage and reached 0.53 A/W at 50 V bias at 222 nm illumination, which corresponds to quantum efficiency higher than 250%, indicating photoconductive gain. The UV/visible rejection ratio reaches seven orders of magnitude at 20 V bias. For sample 2b, responsivity measurements were carried out in the 250–420 nm range. The measured maximum quantum efficiency was 60% at 250 nm, corresponding to 0.12 A/W. The cut-off was

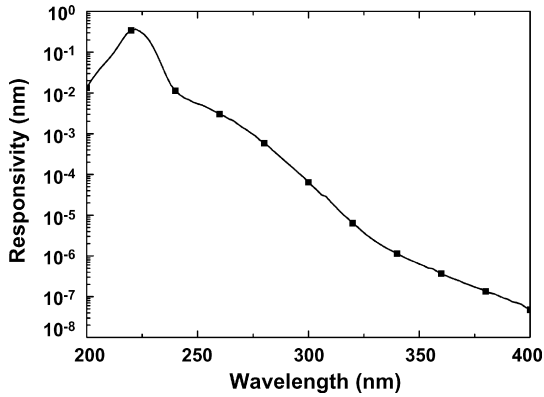Fig. 7. Spectral transmission measurement of sample 2a ($Al_{0.75}Ga_{0.25}N$) and sample 2b ($Al_{0.6}Ga_{0.4}N$).

Fig. 9. Spectral responsivity measurements of a 400 μm × 400 μm MSM photodetector on sample 2a (Al$_{0.75}$Ga$_{0.25}$N). UV/visible rejection ratio reaches 7 orders of magnitude.

Fig. 11. Transmission spectra of sample 3 (two-color MSM photodetector structure) measured for different etch depths.

around 255 nm, which is in good agreement with the transmission data. The UV/visible rejection reached five orders of magnitude for sample 2b [32].

5. Two-color AlGaN MSM photodetectors

The two-color MSM photodetector structure shown in Table 3 incorporates a built-in epitaxial spectral-filter-layer sandwiched between two detector active layers. The device is designed for substrate-side illumination. Fig. 10 is a schematic of the fabricated monolithic two-color UV MSM photodetectors. The bottom detector has the epitaxial layer with the highest band-gap energy (E_{gb}). Light that is not absorbed ($hv < E_{gb}$) in the active layer of the bottom detector travels through the thick spectral filter layer that has an intermediate band-gap energy (E_{gf}). All photons with
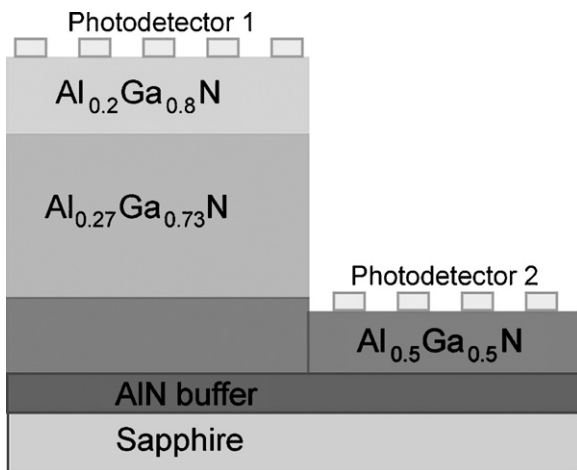

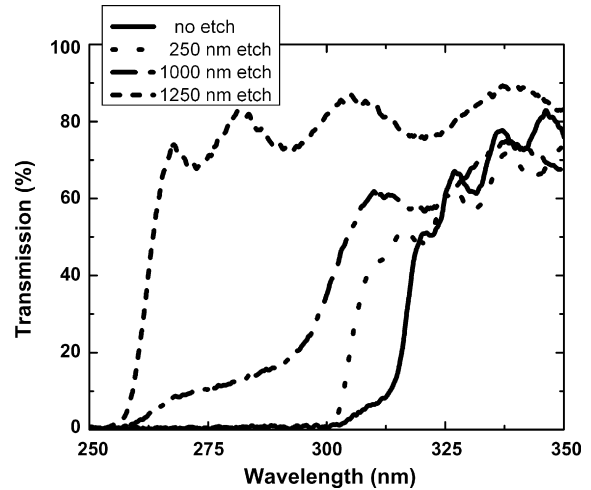Fig. 10. Schematic of fabricated two-color MSM AlGaN photodetectors.

energy $E_{gb} > hv > E_{gf}$ are absorbed closer to the substrate side of the filter layer, while those photons with $hv < E_{gf}$ are transmitted through the filter layer. The thickness of the spectral filter layer is such that the photogenerated carriers in this layer recombine before they can diffuse into the E-field of the top photodetector layer. Therefore, the top photodetector, which has the lowest Al concentration and the lowest band-gap energy (E_{gt}), only detects light with $E_{gf} > hv > E_{gt}$.

The sample was grown as described in Section 2, and transmission spectrum was measured as epitaxial material was removed from the surface progressively by RIE. Fig. 11 shows the spectral transmission measurements of the wafer prior to the surface recess etch, and for three different etch depths. The as-grown wafer exhibited a sharp cut-off at 315 nm due to the top Al$_{0.2}$Ga$_{0.8}$N detector layer. After the top detector layer was removed, the transmission exhibited a sharp cut-off at 301 nm. For a total etch-depth of 1 μm, a partial transmission is observed between 259 nm and 301 nm. This is because the remaining Al$_{0.27}$Ga$_{0.73}$N layer is not thick enough to absorb the entire incident light. Finally, when 1.25 μm of material was removed, the sample exhibited a sharp cut-off at 259 nm in agreement with the Al$_{0.5}$Ga$_{0.5}$N bottom detector layer.

MSM photodetectors were fabricated on sample 3 as described in Section 2. The dark current measured from both the top (fabricated on the as-grown surface) and bottom (fabricated on the recess-etched surface) detectors is shown in Fig. 12. Both detectors were 100 μm × 100 μm area devices with 3 μm/3 μm finger width/spacing. The dark current of the bottom detector was below the dark current of the top detector. The dark

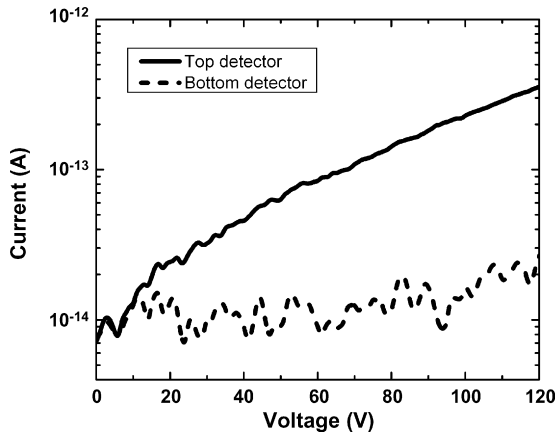Fig. 12. Current–voltage characteristics of $100 \, \mu m \times 100 \, \mu m$ two-color MSM photodetectors with $3 \, \mu m/3 \, \mu m$ finger width/spacing fabricated on sample 3.

current at 0 V bias was 8 fA and 6 fA for top and bottom detectors, respectively. At 50 V, dark current density was 6×10^{-10} A/cm^2 and 1.4×10^{-10} A/cm^2 for the top and bottom detectors, respectively. Both devices exhibited good breakdown characteristics. No sign of breakdown was observed up to 200 V bias. The improved dark current characteristics of the bottom detector can be attributed mainly to the higher Al concentration. Also, this better electrical performance indicates no significant morphological or contact degradation following RIE.

Spectral photoresponse of the top and bottom detectors was measured with the setup described in Section 3, however through the substrate side. It was determined that both devices exhibited bias-dependent responsivity, and the bias values were chosen such that the peak responsivities would be comparable. As seen in
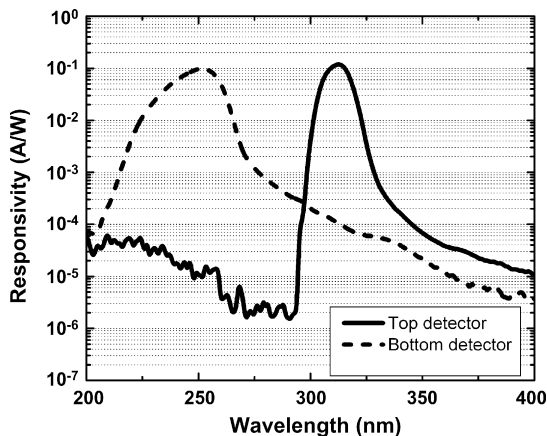

Fig. 13. Photoresponse of $200 \, \mu m \times 200 \, \mu m$ two-color MSM photo-detectors.

Fig. 13, for the top detector, peak of the response is 0.12 A/W for a 10 V bias, which occurs at 310 nm. In comparison, the peak responsivity of the bottom detector is 0.1 A/W at 254 nm for a 25 V bias. The FWHM of the responsivity peak was 11 nm and 22 nm for top and bottom detectors, respectively. Top detector response drops sharply below 300 nm for nearly 5 orders of magnitude due to the absorption in the 1 μm-thick $Al_{0.27}Ga_{0.73}N$ layer, which acts as an absorptive spectral filter. Furthermore, top detector rejects light in bottom detector's operation band with more than 4 orders of magnitude, whereas bottom detector rejects light in top detector's operation band with more than 3 orders of magnitude. In addition, both detectors reject visible light extremely well, with more than 4 orders of rejection.

6. High-speed solar-blind AlGaN MSM photodetectors

The high-speed MSM photodetector structure shown in Table 4 was grown and devices were fabricated as described in Section 2. The current–voltage and spectral photoresponse characteristics were determined as described in Section 3. It was found that, for 10 μm finger width/spacing devices, the dark current density was 1×10^{-6} A/cm^2 and breakdown occurred at 80 V [33]. Spectral photoresponse of the fabricated devices displayed a large photoconductive gain for relatively low bias voltages. The response was solar-blind with a sharp cut-off at 272 nm. The peak responsivity was measured as 1.26 A/W at 264 nm, corresponding to a quantum efficiency of 600%, at 6 V bias.

Temporal response measurements of the solar-blind AlGaN MSM photodetectors were done at 267 nm. A femtosecond mode-locked Ti:sapphire laser was used to generate ultrafast UV pulses by using a two-stage set-up employing two nonlinear BBO (betta barium borate) crystals. The 76 MHz repetition-rate pulse train of 140 fs-long pulses at 800 nm pump wavelength were frequency doubled to generate a second harmonic beam at 400 nm, which in turn was frequency summed by the remaining pump beam in order to generate a third harmonic output beam at 267 nm. The resulting 267 nm pulses had less than 1 ps pulse-widths, and were focused onto the device-under-test using UV-enhanced mirrors and lenses. The resulting high-speed electrical pulse response was observed on a 50 GHz sampling oscilloscope.

The measured time-response signals had very short rise times and exponentially decaying fall times. Devices with smaller finger spacing yielded faster
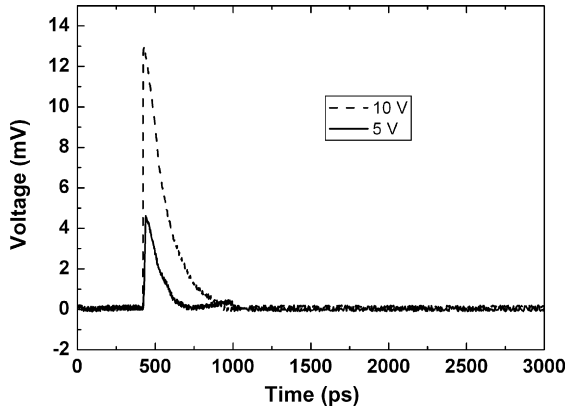
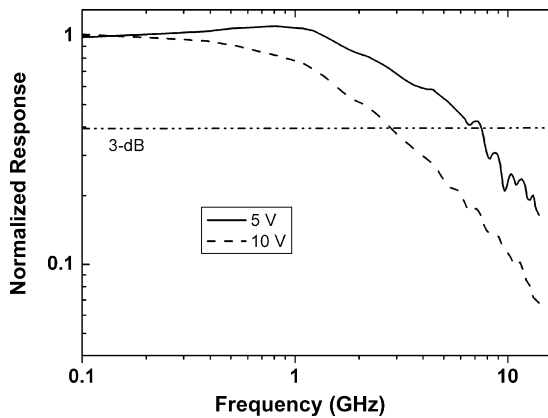Fig. 14. Temporal pulse response of AlGaN MSM photodetectors with 3 μm finger width/spacing.

Fig. 15. Frequency domain response of AlGaN MSM photodetectors obtained by using FFT of the data in Fig. 14.

pulses due to reduced transit times. Therefore, the fastest high-speed response was achieved with 3 μm finger width/spacing devices. Fig. 14 shows the measured pulses from a 3 μm finger width/spacing MSM photodetector for 5 V and 10 V bias, respectively. As bias voltage was increased, both pulse amplitude and pulse width increased resulting in higher amplitude but slower response. The FWHM pulse width value was 99 ps and 121 ps at 5 V and 10 V bias, respectively. The measured pulse waveforms were frequency-analyzed using fast Fourier transform (FFT). Fig. 15 shows the FFT results. Maximum 3-dB bandwidths of 5.4 GHz and 2.1 GHz were obtained at 5 V and 10 V bias, respectively, demonstrating the slowing effect of photoconductive gain.

7. Conclusions

We have designed, grown, fabricated, and char-acterized high-performance AlGaN-based heterojunc-tion MSM photodetectors. The dark current results demonstrated for the GaN MSM photodetectors correspond to the best reported performance. The low cut-off wavelength of $Al_{0.75}Ga_{0.25}N$ photodetec-tors correspond to one of the lowest reported. The 3-dB bandwidth reported is the highest for solar-blind AlGaN MSM photodetectors. Finally, the two-color monolithic MSM photodetectors demonstrated are the first reported.

References

[1] E. Monroy, F. Omnes, F. Calle, Semicond. Sci. Technol. 18 (2003) R33–R51.
[2] M.A. Khan, M. Shatalov, H.P. Maruska, H.M. Wang, E. Kuok-stis, Jpn. J. Appl. Phys. 44 (2005) 7191–7206.
[3] M. Razeghi, A. Rogalsky, J. Appl. Phys. 79 (1996) 7433.
[4] S. Strite, H. Morkoç, J. Vac. Sci. Technol. A 10 (1992) 1237–1266.
[5] H. Morkoc, et al. J. Cryst. Growth 150 (1995) 887–891.
[6] D. Brunner, H. Angerer, E. Bustarret, F. Freudenberg, R. Höpler, R. Dimitrov, O. Ambacher, M. Stutzmann, J. Appl. Phys. 82 (1997) 5090–5096.
[7] F. Omnès, N. Marenco, B. Beaumont, Ph. de Mierry, E. Monroy, F. Calle, E. Muñoz, J. Appl. Phys. 86 (1999) 5286–5292.
[8] S.C. Jain, M. Willander, J. Narayan, R. Van Overstraeten, J. Appl. Phys. 87 (2000) 965–1006.
[9] J.P. Zhang, H.M. Wang, M.E. Gaevski, C.Q. Chen, Q. Fareed, J.W. Yang, G. Simin, M.A. Khan, Appl. Phys. Lett. 80 (2002) 3542–3544.
[10] C.Q. Chen, J.P. Zhang, M.E. Gaevski, H.M. Wang, W.H. Sun, R.S.Q. Fareed, J.W. Yang, M.A. Khan, Appl. Phys. Lett. 81 (2002) 4961–4963.
[11] M.A. Khan, J. Kuznia, D.T. Olson, M. Blasingame, A.R. Bhat-tarai, Appl. Phys. Lett. 63 (1993) 2455.
[12] D. Walker, X. Zhang, P. Kung, A. Saxler, S. Javapor, J. Xu, M. Razeghi, Appl. Phys. Lett. 68 (1996) 2100–2101.
[13] B.W. Lim, Q.C. Chen, J.Y. Yang, M.A. Khan, Appl. Phys. Lett. 68 (1996) 3761–3762.
[14] A. Osinsky, S. Gangopadhyay, B.W. Lim, M.Z. Anwar, M.A. Khan, D.V. Kuksenkov, H. Temkin, Appl. Phys. Lett. 72 (1998) 742–744.
[15] E. Monroy, F. Calle, J.L. Pau, F.J. Sanchez, E. Munoz, F. Omnes, B. Beaumont, P. Gibart, J. Appl. Phys. 88 (2000) 2081–2091.
[16] N. Biyikli, I. Kimukin, T. Tut, O. Aytur, E. Ozbay, Appl. Phys. Lett. 81 (2002) 3272.
[17] G. Parish, S. Keller, P. Kozodoy, J.P. Ibbetson, H. Marchand, P.T. Fini, S.B. Fleischer, S.P. Denbaars, U.K. Mishra, E.J. Tarsa, Appl. Phys. Lett. 75 (1999) 247–249.

[18] D.J.H. Lambert, M.M. Wong, U. Chowdhury, C. Collins, T. Li, H.K. Kwon, B.S. Shelton, T.G. Zhu, J.C. Campbell, R.D. Dupuis, Appl. Phys. Lett. 77 (2000) 1900–1902.

[19] P. Sandvik, K. Mi, F. Shahedipour, R. McClintock, A. Yasan, P. Kung, M. Razeghi, J. Cryst. Growth 231 (2001) 366–370.

[20] A. Hirano, C. Pernot, M. Iwaya, T. Detchprohm, H. Amano, I. Akasaki, Phys. Stat. Sol. (A) 188 (2001) 293–296.

[21] V.V. Kuryatkov, H. Temkin, J.C. Campbell, R.D. Dupuis, Appl. Phys. Lett. 78 (2001) 3340–3342.

[22] U. Chowdhury, M.M. Wong, C.J. Collins, B. Yang, J.C. Denyszyn, J.C. Campbell, R.D. Dupuis, J. Cryst. Growth 248 (2003) 552–555.

[23] E. Ozbay, N. Biyikli, İ. Kimukin, T. Kartaloglu, T. Tut, O. Aytür, IEEE J. Sel. Top. Quantum Electron. 10 (2004) 742–751.

[24] T. Li, D.J.H. Lambert, A.L. Beck, C.J. Collins, B. Yang, J.M.M. Wong, U. Chowdhury, R.D. Dupuis, J.C. Campbell, Electron. Lett. 36 (2000) 1581.

[25] J.Y. Duboz, J.L. Reverchon, D. Adam, B. Damilano, N. Grandjean, F. Semond, J. Massies, J. Appl. Phys. 92 (2002) 5602.

[26] R. McClintock, A. Yasan, K. Minder, P. Kung, M. Razeghi, Appl. Phys. Lett. 87 (2005) 241123.

[27] T. Tut, M. Gokkavas, B. Butun, S. Butun, E. Ulker, E. Ozbay, Appl. Phys. Lett. 89 (2006) 183524.

[28] E. Monroy, F. Calle, E. Munoz, F. Omnes, Appl. Phys. Lett. 74 (1999) 3401.

[29] E. Monroy, T. Palacios, O. Hainaut, F. Omnes, F. Calle, J.F. Hochedez, Appl. Phys. Lett. 80 (2002) 3198.

[30] M. Ito, O. Wada, K. Nakai, T. Sakurai, IEEE Electron Device Lett. 5 (1984) 531.

[31] D. Walker, V. Kumar, K. Mi, P. Sandvik, P. Kung, X.H. Zhang, M. Razeghi, Appl. Phys. Lett. 76 (2000) 403.

[32] N. Biyikli, I. Kimukin, T. Kartaloglu, O. Aytur, E. Ozbay, Electron. Lett. 41 (2005) 276.

[33] N. Biyikli, I. Kimukin, T. Kartaloglu, O. Aytur, E. Ozbay, Phys. Stat. Sol. (c) 7 (2003) 2314–2317.